



# Inflation and burst of aluminum tubes. Part II: An advanced yield function including deformation-induced anisotropy

Yannis P. Korkolis, Stelios Kyriakides \*

*Research Center for Mechanics of Solids, Structures and Materials, WRW 110, C0600,  
The University of Texas at Austin, WRW 110, Austin, TX 78712, United States*

Received 14 September 2007; received in final revised form 27 February 2008  
Available online 14 March 2008

---

## Abstract

In a recent study [Korkolis, Y.P., Kyriakides, S., 2008. Inflation and burst of anisotropic aluminum tubes for hydroforming applications. *Int'l. J. Plasticity* 24, 509–543], the formability of aluminum tubes was investigated using a combination of experimental and numerical approaches. The tubes were loaded to failure under combined internal pressure and axial load along radial paths in the engineering stress space. The experiments were then simulated using appropriate FE models and two established anisotropic yield functions. It was found that for some loading paths the computed deformations did not agree with the experimental ones, whereas rupture was generally over-predicted. In the current study the problem is tackled using a more advanced yield function [Barlat, F., Brem, J.C., Yoon, J.W., Chung, K., Dick, R.E., Lege, D.J., Pourboghrat, F., Choi, S.-H., Chu, E., 2003. Plane stress function for aluminum alloy sheets – part I: theory. *Int'l. J. Plasticity* 19, 1297–1319]. Three different calibration schemes of this function are employed, in two of which the experimentally observed deformation-induced anisotropy is taken into account. It is demonstrated that both deformation and failure can ultimately be predicted successfully, albeit arduously, using a hybrid procedure detailed herein.

© 2008 Elsevier Ltd. All rights reserved.

*Keywords:* Aluminum; Tube hydroforming; Burst; Deformation-induced anisotropy

---

\* Corresponding author. Tel.: +1 5124714167; fax: +1 5124715500.  
E-mail address: [skk@mail.utexas.edu](mailto:skk@mail.utexas.edu) (S. Kyriakides).

## 1. Introduction

A series of tests have recently been conducted involving Al-6260-T4 tubes inflated under combined internal pressure and axial load (Korkolis and Kyriakides, 2008). The tubes were loaded to failure along radial paths in the engineering stress space. Hill-type plastic work contours (Hill et al., 1994) were constructed from the results, which indicated some deformation-induced anisotropy. The specimens developed localized axisymmetric bulging associated with a limit load. The loading scheme followed enabled control of the test past that instability, to localized failure. In axial tension dominant loading paths the tubes failed by circumferential rupture. For hoop stress dominant paths the rupture was along a tube generator (see Kuwabara et al., 2005 for similar experiments). The experiments were then simulated with finite element (FE) models in which Hosford's (1979) and Karafillis and Boyce's (1993) anisotropic yield functions were employed, using an associated flow rule and isotropic hardening. Two distinct FE models were developed, each tailored to simulate either axial or circumferential rupture. The two yield functions were calibrated not only to the plastic work contours, but also with regards to the successful prediction of the limit load states (loads and deformations). The simulations revealed some deficiencies of these constitutive models. First, the induced strain paths were not uniformly predicted with sufficient accuracy and second, the onset of failure was uniformly overpredicted. In this brief note the subject is revisited using the same FE models but incorporating a more powerful anisotropic yield function (Barlat et al., 2003). The effect of the evolution of the anisotropy is now also investigated.

## 2. Constitutive modeling: yield function Yld2000-2D (Barlat et al., 2003)

Hosford's (1972) isotropic yield function in terms of the principal stress deviators can be written as

$$|s_1 - s_2|^k + |2s_1 + s_2|^k + |s_1 + 2s_2|^k = 2\sigma_0^k. \quad (1)$$

Barlat et al. introduced anisotropy by two linear transformations, one applied to the first term ( $\phi'$ ) and the other to the second and third terms ( $\phi''$ ):

$$\phi = \phi' + \phi'' = |S'_1 - S'_2|^k + |2S''_1 + S''_2|^k + |S''_1 + 2S''_2|^k = 2\sigma_0^k. \quad (2)$$

Here ( $S'_1, S'_2$ ) and ( $S''_1, S''_2$ ) are the principal values of the linearly transformed stress tensors  $S'$  and  $S''$ , respectively. These tensors are obtained from the stress deviator  $s$  and the stress tensor  $\sigma$  by:

$$S' = C's = C'T\sigma = L'\sigma \quad \text{and} \quad S'' = C''s = C''T\sigma = L''\sigma \quad (3)$$

where  $C$ ,  $C'$ ,  $T$ ,  $L'$  and  $L''$  are appropriate transformation tensors that allow introduction of the anisotropy (Barlat et al., 2003). Thus, for our 2-D stress state

$$\begin{Bmatrix} S'_x \\ S'_y \\ S'_{xy} \end{Bmatrix} = \begin{bmatrix} L'_{11} & L'_{12} & 0 \\ L'_{21} & L'_{22} & 0 \\ 0 & 0 & L'_{66} \end{bmatrix} \begin{Bmatrix} \sigma_x \\ \sigma_y \\ \sigma_{xy} \end{Bmatrix} \quad \text{and} \quad \begin{Bmatrix} S''_x \\ S''_y \\ S''_{xy} \end{Bmatrix} = \begin{bmatrix} L''_{11} & L''_{12} & 0 \\ L''_{21} & L''_{22} & 0 \\ 0 & 0 & L''_{66} \end{bmatrix} \begin{Bmatrix} \sigma_x \\ \sigma_y \\ \sigma_{xy} \end{Bmatrix} \quad (4a)$$

where  $L'$  and  $L''$  are related to parameters  $\alpha_i$  ( $i = 1, 8$ ) as follows:

$$\begin{pmatrix} L'_{11} \\ L'_{12} \\ L'_{21} \\ L'_{22} \\ L'_{66} \end{pmatrix} = \begin{bmatrix} 2/3 & 0 & 0 \\ -1/3 & 0 & 0 \\ 0 & -1/3 & 0 \\ 0 & 2/3 & 0 \\ 0 & 0 & 1 \end{bmatrix} \begin{pmatrix} \alpha_1 \\ \alpha_2 \\ \alpha_7 \end{pmatrix} \quad \text{and} \quad \begin{pmatrix} L''_{11} \\ L''_{12} \\ L''_{21} \\ L''_{22} \\ L''_{66} \end{pmatrix} = \frac{1}{9} \begin{bmatrix} -2 & 2 & 8 & -20 \\ 1 & -4 & -4 & 40 \\ 4 & -4 & -4 & 10 \\ -2 & 8 & 2 & -20 \\ 0 & 0 & 0 & 09 \end{bmatrix} \begin{pmatrix} \alpha_3 \\ \alpha_4 \\ \alpha_5 \\ \alpha_6 \\ \alpha_8 \end{pmatrix}. \quad (4b)$$

(The first and second derivatives of the yield function with respect to the stress components required for the flow rule and its numerical implementation appear in Barlat et al. (2003) and Yoon et al. (2004)).

The exponent  $k$  is assigned the value of 8 as is typical for aluminum alloys. The model is then calibrated by fitting the parameters  $\alpha_i$  ( $i = 1, 8$ ) to the experimental work contours. Of these  $\alpha_7$  and  $\alpha_8$  are related to the shear stresses. Korkolis and Kyriakides (2008) demonstrated that shear anisotropy does not influence the predictions of this set of biaxial burst experiments and as a result it will be neglected here too (i.e.,  $\alpha_7 = \alpha_8 = 1$ ). Three different calibration schemes were attempted, leading to different performance first in predicting the strain paths traced and second in identifying the onset of rupture. The three methods of calibration and the results are discussed in the next section.

### 3. Model calibration and performance

#### 3.1. Case I

In this case, in view of the experimentally observed evolution of the plastic work contours we found it more convenient to choose the anisotropy variables from a subsequent work contour,  $W^p = 2$  ksi (13.8 MPa). The  $\alpha_i$  were chosen for best fit of the experimental data and are given in Table 1. Fig. 1a shows a plot of the experimental data normalized by the flow stress in uniaxial tension along with the yield surface calibrated in this manner (solid line). The comparison is seen to be quite favorable. The whole set of work contours is compared to the corresponding experimental data in Fig. 1b. It can be observed that this calibration procedure resulted in a very good fit of the data for  $W^p = 2$  ksi (13.8 MPa), while the agreement is slightly more adverse for other contours but better than the corresponding results from the Hosford (Fig. 17 in Korkolis and Kyriakides, 2008) and the Karafillis–Boyce (Fig. 18b in Korkolis and Kyriakides, 2008) yield functions.

The calibrated yield function was implemented in the FE models of Korkolis and Kyriakides (2008) and the nine experiments were simulated. Fig. 2 shows the calculated (engineering) strain paths, in each case truncated at the corresponding limit load. By comparison to the corresponding results in Figs. 27 and 29 in Korkolis and Kyriakides (2008),

Table 1  
Anisotropy parameters for Case I

$W^p$	$\alpha_1$	$\alpha_2$	$\alpha_3$	$\alpha_4$	$\alpha_5$	$\alpha_6$	$\alpha_7$	$\alpha_8$
2 ksi	0.78	1.15	0.85	0.89	1.06	1.03	1.0	1.0

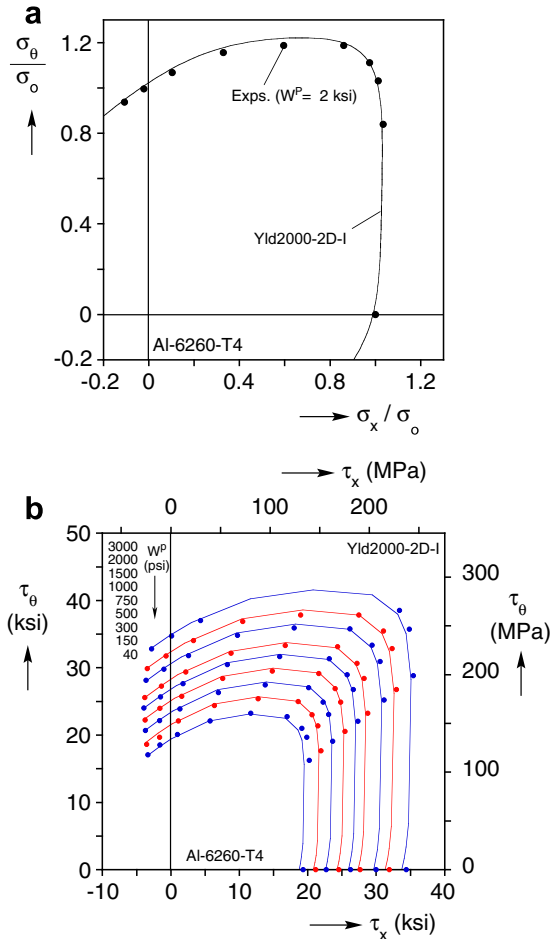


Fig. 1. (a) Experimental data representing the 2 ksi (13.8 MPa) work contour and the Yld2000-2D yield function, Case I. (b) Loci of experimental points representing various levels of constant plastic work and corresponding contours based on the Yld2000-2D yield function, Case I.

the paths are now uniformly closer to the experimental ones, although the paths predicted for  $\alpha = 1$  and 0.9 maintain some difference from the experimental ones. The improvement in performance can be linked to the better agreement between the shapes of the calibrated and measured work contours. This, of course, is a direct consequence of the increased flexibility (eight parameters) provided by the Yld2000-2D yield function over Hosford's (1979) (two parameters) and Karafillis and Boyce's (1993) (four parameters) (see Figs. 17 and 18b in Korkolis and Kyriakides (2008)). Despite this improvement, the onset of the limit loads is delayed and the corresponding strains (ends of trajectories) are much larger than the experimental ones. Consequently, the calculated onsets of rupture are similarly delayed as seen in Fig. 3 for the failure strains. (Note that in this plot both the experimental and the computed values are averaged over the extensometer gage lengths as described in Korkolis and Kyriakides (2008) Section 2.2 pp. 522–523 and Section 4.2 pp. 531–532.)

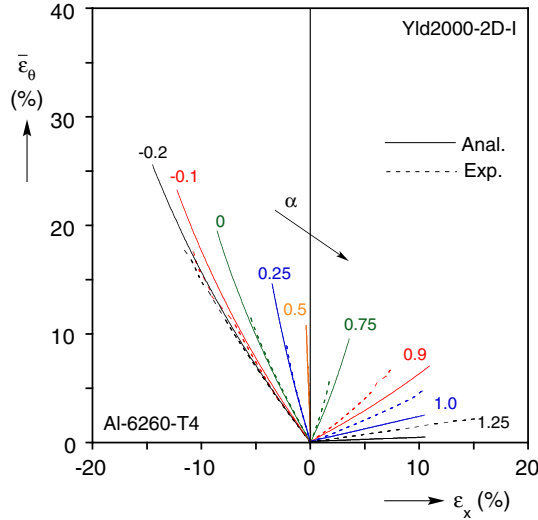


Fig. 2. Comparison of calculated and measured engineering strain paths for nine loading cases using the Yld2000-2D yield function, Case I.

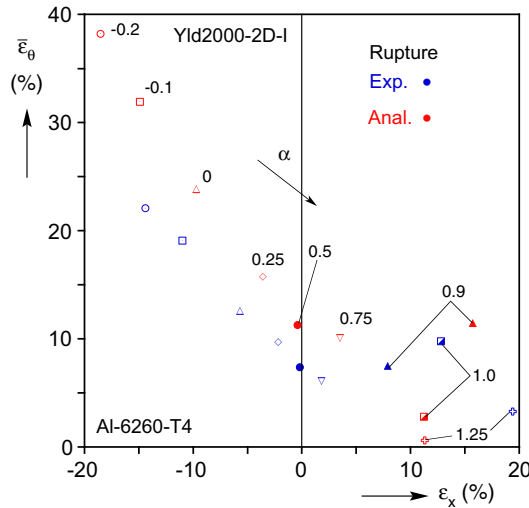


Fig. 3. Comparison of measured and calculated average strains at rupture using the Yld2000-2D yield function, Case I.

### 3.2. Case II

Encouraged by the improvement provided by the Yld2000-2D yield function in the prediction of the strain paths, in a second attempt the coefficients  $\alpha_i$  are allowed to change with increasing plastic deformation (Plunkett et al., 2006). This is done in order to also account for the experimentally observed deformation-induced anisotropy. The calibration was performed as follows. For six of the experimental work contours (9.2, 150, 500, 1000,

2000 and 3000 psi–0.0635, 1.03, 3.45, 6.9, 13.8, 20.7 MPa) the anisotropy parameters were selected for best fit of each contour. The resulting  $\alpha_i$  are given in Table 2 while the fitted contours are presented in Fig. 4, where it can be noted that the agreement to the experimental data is somewhat improved over that in Fig. 1.

In the FE implementation of the model, for each value of the plastic work the corresponding parameters are determined by linear interpolation between two neighboring contours. The calculated strain paths are compared to the measured ones in Fig. 5. The computed results in general follow the experiments with small deviations in the equibiaxial region. It is quite possible that additional data may be required in this high curvature area for further improvement of these predictions. It is interesting to observe that the results in Fig. 5 do not differ significantly from the results of Case I (Fig. 2). This is partly due to the fact that the evolution of anisotropy is mild for this material, and partly due to the fitting of Case I to a subsequent work contour rather than to the initial yield surface. Unfortunately, the predicted limit loads (ends of paths) are delayed essentially to the same extent as those in Fig. 2. The same is true for the failure strains plotted with the corresponding experimental values in Fig. 6. This state of affairs confirms that matching of the work con-

Table 2  
Anisotropy parameters for Case II

$W^p$	$\alpha_1$	$\alpha_2$	$\alpha_3$	$\alpha_4$	$\alpha_5$	$\alpha_6$	$\alpha_7$	$\alpha_8$
9.2 psi	0.88	1.15	0.87	0.91	1.03	1.01	1.0	1.0
150 psi	0.8	1.15	0.92	0.88	1.05	1.03	1.0	1.0
500 psi	0.83	1.12	0.85	0.87	1.05	1.03	1.0	1.0
1 ksi	0.83	1.15	0.85	0.88	1.05	1.03	1.0	1.0
2 ksi	0.78	1.15	0.85	0.89	1.06	1.03	1.0	1.0
3 ksi	0.74	1.18	0.85	0.89	1.06	1.03	1.0	1.0

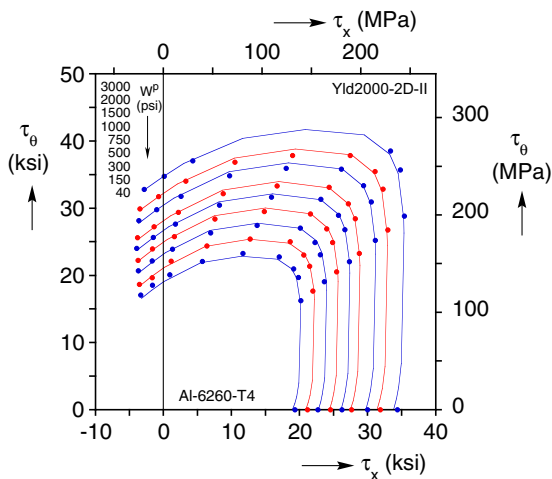


Fig. 4. Loci of experimental points representing various levels of constant plastic work and corresponding contours based on the Yld2000-2D yield function, Case II.

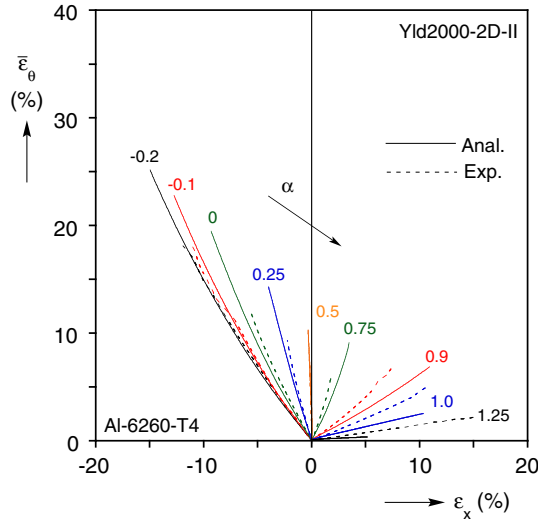


Fig. 5. Comparison of calculated and measured engineering strain paths for nine loading cases using the Yld2000-2D yield function, Case II.

tours closely improves the prediction of the strain paths but is not by itself sufficient to ensure accurate prediction of failure.

### 3.3. Case III

In an effort to understand the extent to which the calibrated yield functions used above need to be modified for the model predictions of the failure strains to approach the

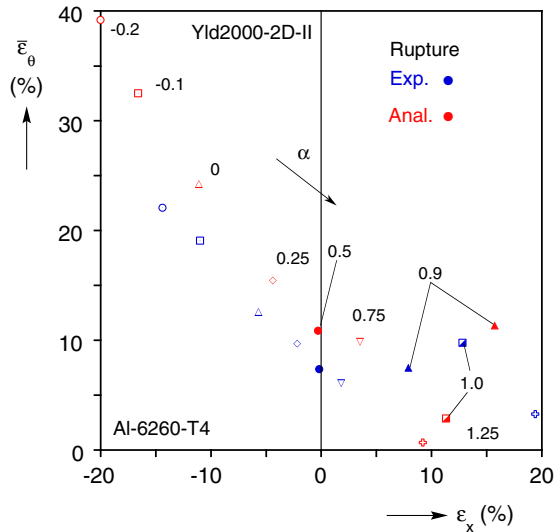


Fig. 6. Comparison of measured and calculated average strains at rupture using the Yld2000-2D yield function, Case II.

measured values, the following “hybrid” calibration approach was employed. The parameters given in Table 2 were considered as an initial guess for an iterative procedure where they were re-adjusted until an acceptable structural performance was achieved. The main structural performance criteria used were the loads and strains at which the limit load was

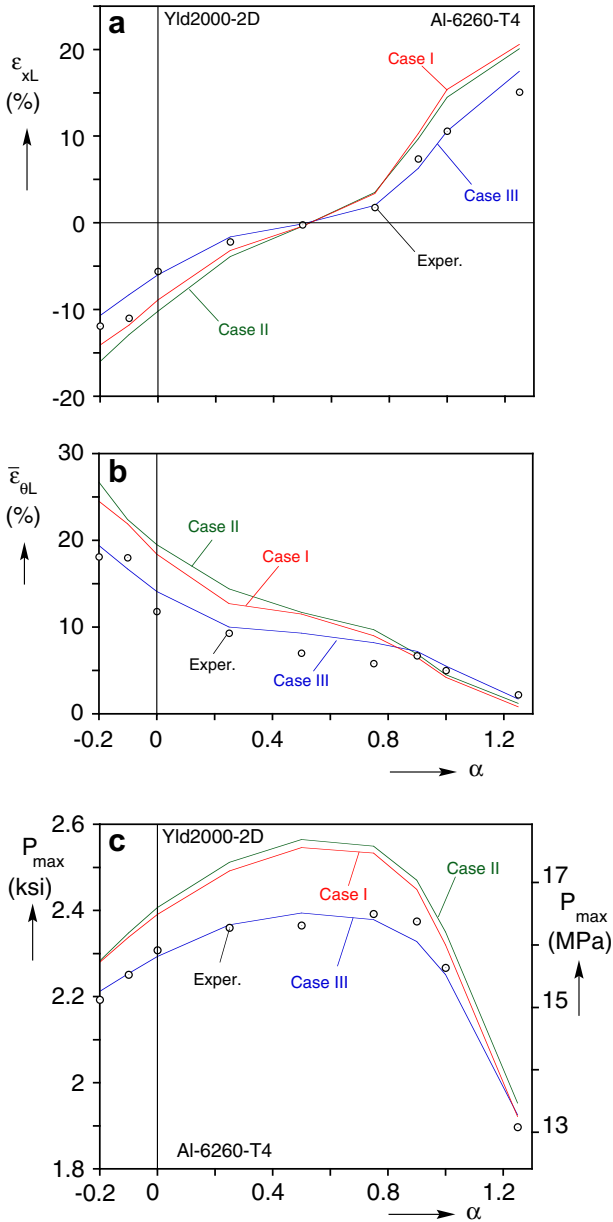


Fig. 7. Performance of the three constitutive models in predicting the limit load states for each imposed stress ratio  $\alpha$  and corresponding experimental data. (a) Axial strain at the limit pressure, (b) hoop strain at the limit pressure, and (c) limit pressure.

attained. Fig. 7 shows the axial (a) and circumferential strains (b) at the limit loads measured in the experiments as a function of the loading parameter  $\alpha$  ( $=\sigma_x/\sigma_\theta$ ). Included are the corresponding values predicted using the constitutive models of Cases I and II. Both are seen to deviate from the experimental values by a certain degree. The two models also overpredict the corresponding limit pressures ( $P_{max}$ ) shown in Fig. 7c.

To improve this performance, the parameters were iteratively readjusted by performing a number of structural runs (note that an axisymmetric model suffices for this purpose) in each case modifying the yield function parameters  $\alpha_i$  to approach the experimental data at the limit load. The values of  $\alpha_i$  found to produce optimal overall results are given in Table 3. The calculated strains and pressures that correspond to the limit loads are included in Fig. 7 and are seen to be in much better agreement with the experimental values than Cases I or II. Even though the work contours of Case III shown in Fig. 8 now deviate somewhat from the experimental values, the induced strain paths shown in Fig. 9 are very close to the experimental ones. Furthermore, the limit load states (ends of trajectories) are quite close to the actual ones. Indeed, they are much closer than any results obtained pre-

Table 3  
Anisotropy parameters for Case III

$W^p$	$\alpha_1$	$\alpha_2$	$\alpha_3$	$\alpha_4$	$\alpha_5$	$\alpha_6$	$\alpha_7$	$\alpha_8$
9.2 psi	0.917	1.066	0.92	0.935	1.018	0.993	1.0	1.0
150 psi	0.87	1.066	0.92	0.91	1.05	1.03	1.0	1.0
500 psi	0.87	1.066	0.85	0.92	1.05	1.03	1.0	1.0
1 ksi	0.88	1.066	0.91	0.91	1.035	1.01	1.0	1.0
2 ksi	0.88	1.066	0.94	0.94	1.04	1.01	1.0	1.0
3 ksi	0.88	1.05	0.92	0.97	1.05	1.06	1.0	1.0

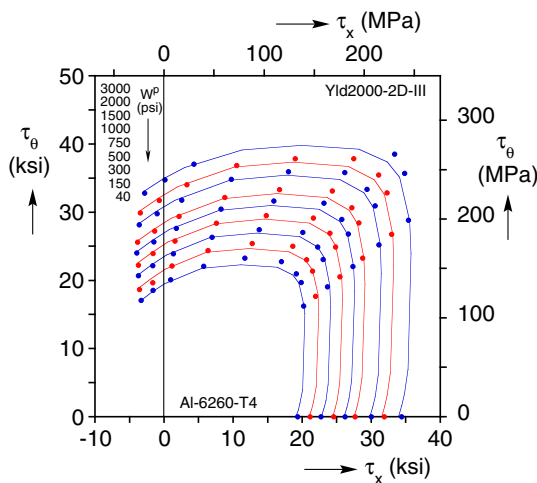


Fig. 8. Loci of experimental points representing various levels of constant plastic work and corresponding contours based on the Yld2000-2D yield function, Case III.

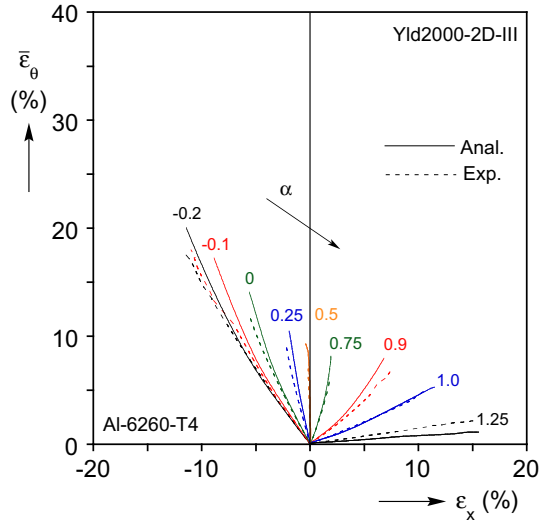


Fig. 9. Comparison of calculated and measured engineering strain paths for nine loading cases using the Yld2000-2D yield function, Case III.

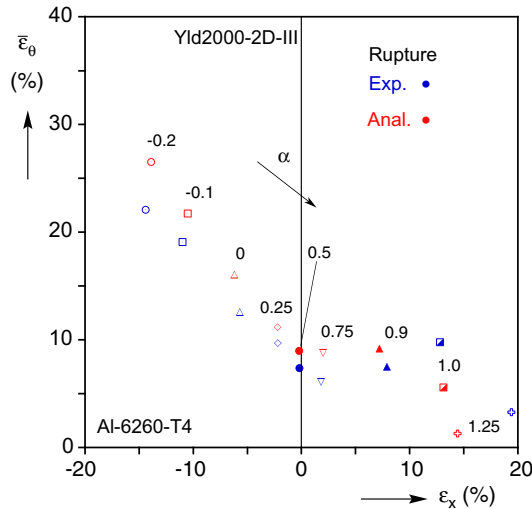


Fig. 10. Comparison of measured and calculated average strains at rupture using the Yld2000-2D yield function, Case III.

viously, either in this work or in Korkolis and Kyriakides (2008). This uniformly improved performance also carries on to the calculated failure strains, shown in Fig. 10. It is interesting to observe that the work contours produced by this hybrid scheme do not seem markedly different from those of Cases I and II (Figs. 1b and 4). However, the small shape changes introduced were sufficient to improve the predictions of failure.

For completeness for this case the engineering stress paths prescribed are shown in Fig. 11. Marked on the trajectories are the predicted stresses at the limit loads (●) and

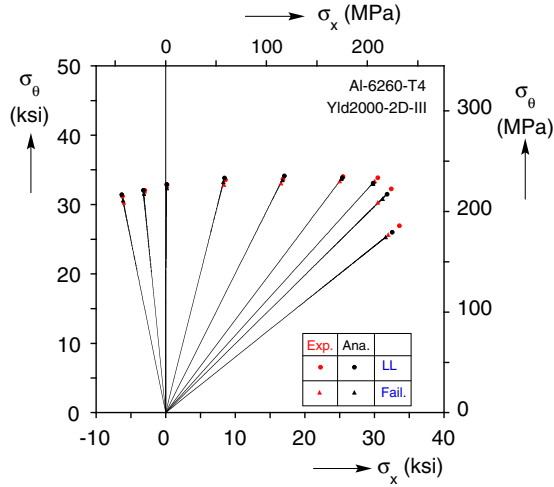


Fig. 11. Engineering stress paths prescribed. Marked are the stresses at the limit load and at rupture (predicted and experimental).

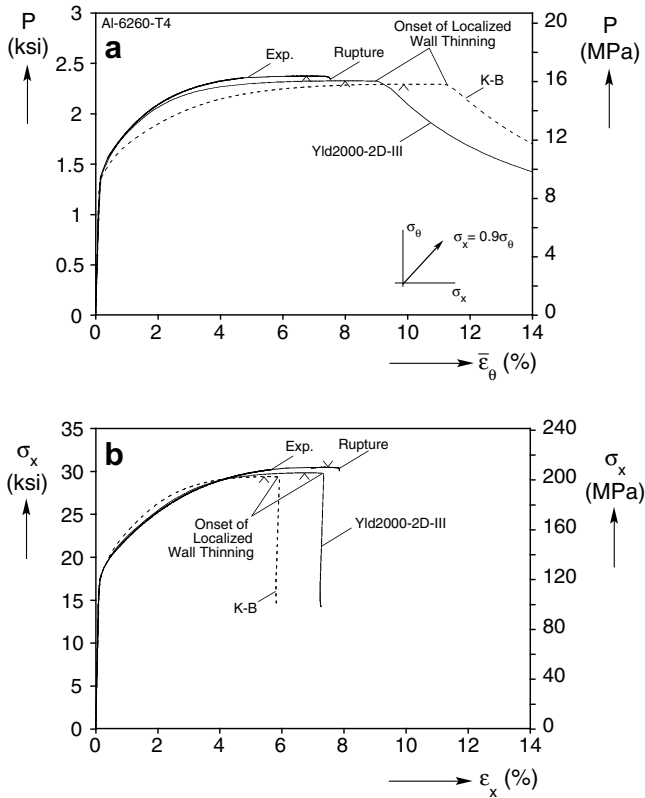


Fig. 12. Results from numerical simulation of experiment for  $\alpha = 0.9$ . (a)  $P-\bar{\epsilon}_\theta$  responses using two plasticity models and the corresponding experimental response. (b)  $\sigma_x-\epsilon_x$  responses using two plasticity models and the corresponding experimental one.

at the onset of rupture ( $\blacktriangle$ ) and the corresponding experimental values (red color)<sup>1</sup>. Both envelopes are seen to agree well with the experimental ones.

A detailed example of this improved performance is shown Fig. 12 where the measured and calculated responses for the case with  $\sigma_x = 0.9\sigma_\theta$  are compared. Fig. 12a shows the pressure-average circumferential strain responses (see Korkolis and Kyriakides, 2008 for definition of  $\bar{\epsilon}_\theta$ ) and Fig. 12b the corresponding axial stress–strain ones. Included in the figure are the predictions obtained using the Karafillis and Boyce's (1993) yield function (Korkolis and Kyriakides, 2008). The first observation is that the Yld2000-2D-III responses are in better agreement to the measured ones than those yielded by Karafillis and Boyce's (1993). The second is that the limit pressure and the onset of localized thinning are both attained at strains that are closer to the experimental values and simultaneously smaller than those of the Karafillis and Boyce's (1993) predictions. This carries over to most of the nine loading paths examined.

#### 4. Conclusions

The inflation and burst of Al-6260-T4 tubes under combined internal pressure and axial load was recently investigated through a combination of experiments and modeling (Korkolis and Kyriakides, 2008). Nine tubes were loaded to rupture following radial paths in the circumferential–axial engineering stress plane. The study revealed some deficiencies of established non-quadratic anisotropic yield functions. First, some of the induced strain paths were not predicted with accuracy and second, the strains at the onset of rupture were generally overpredicted. This unsatisfactory performance could be attributed, at least partly, to the inability of the yield functions adopted to fully capture the anisotropy of the material and its evolution with deformation. In the present extension of this work, an anisotropic yield function with more degrees of freedom (Yld2000-2D) has been implemented in the FE models and its performance has been evaluated.

The Yld2000-2D yield function was calibrated to the data using three different schemes. In the first no evolution was assumed, and the eight anisotropy parameters were selected for good fit of the 2 ksi (13.8 MPa) experimental plastic work contour. This approach improved the predicted strain paths in comparison to Hosford's (1979) or Karafillis and Boyce's (1993), but not the rupture predictions. In the second scheme the evolution of the work contours with plastic deformation was also taken into account. Here the strain paths were further improved slightly but the predicted rupture strains remained unsatisfactory. In the last scheme, the evolution was taken into account but the anisotropy constants were also adjusted for improved overall structural performance. This hybrid calibration resulted in successful predictions of both the deformation and the stresses and strains at rupture.

Clearly, the added flexibility provided by the eight parameters of the Yld2000-2D model enables better fitting of the initial yielding and its evolution. This in turn is responsible for the overall better prediction of the strain paths compared to previously used models with fewer parameters. Nevertheless, this was not by itself sufficient for a corresponding improvement in the predicted rupture strains. A hybrid calibration procedure in which the yield function constants were also iteratively updated by monitoring the structural

<sup>1</sup> For interpretation of color in Fig. 11, the reader is referred to the web version of this article.

response had to be implemented for best overall performance. The work contours corresponding to the optimized model differ slightly from the experimental ones as well as from those of the Yld2000-2D Cases I and II. This indicates that failure is very sensitive to small changes in the yield function. However, the calibration procedure adopted is clearly too cumbersome for implementation in more complex settings.

The difficulties encountered in achieving optimal overall performance of the simulations are most probably linked to the adoption of isotropic hardening in the modeling. Rupture is sensitive to the actual shape of the current yield surface, which is known to both translate and deform. Such features are of course not captured by isotropic hardening plasticity, indicating that more advanced models that capture such evolution characteristics combined with modern anisotropic yield functions are desirable (e.g., see Choi et al., 2006).

## Acknowledgements

The authors acknowledge with thanks financial support of this work received from the National Science Foundation through Grant DMI-0140599 and supplementary funding provided by G.M. with Robin Stevenson as coordinator. Special thanks to Alcoa and Edmund Chu for providing initial seed funding for the project and the tubes analyzed and tested. Discussions with Frederic Barlat of Alcoa were instrumental in the adoption of the Yld2000-2D yield function.

## References

- Barlat, F., Brem, J.C., Yoon, J.W., Chung, K., Dick, R.E., Lege, D.J., Pourboghrat, F., Choi, S.-H., Chu, E., 2003. Plane stress function for aluminum alloy sheets – part I: theory. *Int'l. J. Plasticity* 19, 1297–1319.
- Choi, Y., Han, C.-S., Lee, J.K., Wagoner, R.H., 2006. Modeling multi-axial deformation of planar anisotropic elasto-plastic materials, part I: theory. *Int'l. J. Plasticity* 22, 1745–1764.
- Hill, R., Hecker, S.S., Stout, M.G., 1994. An investigation of plastic flow and differential work hardening in orthotropic brass tubes under fluid pressure and axial load. *Int'l. J. Solids Struct.* 21, 2999–3021.
- Hosford, W.F., 1972. A generalized isotropic yield criterion. *ASME J. Appl. Mech.* 309, 607–609.
- Hosford, W.F., 1979. On yield loci of anisotropic cubic metals. In: *Proc. 7th North Amer. Metalworking Research Conf., Society of Manufacturing Engineers, Dearborn, MI*, pp. 191–196.
- Karafillis, A.P., Boyce, M.C., 1993. A general anisotropic yield criterion using bounds and a transformation weighting tensor. *J. Mech. Phys. Solids* 41, 1859–1886.
- Korkolis, Y.P., Kyriakides, S., 2008. Inflation and burst of anisotropic aluminum tubes for hydroforming applications. *Int'l. J. Plasticity* 24, 509–543.
- Kuwabara, T., Yoshida, K., Narihara, K., Takahashi, S., 2005. Anisotropic plastic deformation of extruded aluminum alloy tube under axial forces and internal pressure. *Int'l. J. Plasticity* 21, 101–117.
- Plunkett, B., Lebensohn, R.A., Cazacu, O., Barlat, F., 2006. Anisotropic yield function of hexagonal materials taking into account texture development and anisotropic hardening. *Acta Mater.* 54, 4159–4169.
- Yoon, J.W., Barlat, F., Dick, R.E., Chung, K., Kang, T.J., 2004. Plane stress function for aluminum alloy sheets – part II: FE formulation and its implementation. *Int'l. J. Plasticity* 20, 495–522.